

Self-Adversarial Training incorporating Forgery Attention for Image Forgery Localization

Long Zhuo, Shunquan Tan*, *Senior Member, IEEE*, Bin Li, *Senior Member, IEEE*, and Jiwu Huang, *Fellow, IEEE*

Abstract—Image editing techniques enable people to modify the content of an image without leaving visual traces and thus may cause serious security risks. Hence the detection and localization of these forgeries become quite necessary and challenging. Furthermore, unlike other tasks with extensive data, there is usually a lack of annotated forged images for training due to annotation difficulties. In this paper, we propose a self-adversarial training strategy and a reliable coarse-to-fine network that utilizes a self-attention mechanism to localize forged regions in forgery images. The self-attention module is based on a Channel-Wise High Pass Filter block (CW-HPF). CW-HPF leverages inter-channel relationships of features and extracts noise features by high pass filters. Based on the CW-HPF, a self-attention mechanism, called *forgery attention*, is proposed to capture rich contextual dependencies of intrinsic inconsistency extracted from tampered regions. Specifically, we append two types of attention modules on top of CW-HPF respectively to model internal interdependencies in spatial dimension and external dependencies among channels. We exploit a coarse-to-fine network to enhance the noise inconsistency between original and tampered regions. More importantly, to address the issue of insufficient training data, we design a self-adversarial training strategy that expands training data dynamically to achieve more robust performance. Specifically, in each training iteration, we perform adversarial attacks against our network to generate adversarial examples and train our model on them. Extensive experimental results demonstrate that our proposed algorithm steadily outperforms state-of-the-art methods by a clear margin in different benchmark datasets.

Index Terms—Forgery localization, forgery attention, coarse-to-fine network, self-adversarial training.

I. INTRODUCTION

THE prevalence of digital image forgery is negatively affecting our lives, such as Internet rumors, insurance fraud, fake news, and even academic cheating [1]. Ghanim and Nabil [2] revealed that image forgery might cause huge financial loss. Bik *et al.* [3] estimated that there were 3.8% of 20,621 papers containing problematic figures with potential

deliberate manipulation in biomedical research publications. Yet, the majority cases of image forgeries have not been detected [4] due to the fact that image manipulation is very difficult to detect, and tampered images are commonly indistinguishable from original images by naked eyes. With the automatic generation techniques (e.g., inpainting with generative adversarial networks) and popular image editing tools (such as Photoshop®, After Effects Pro®, and the open-source software GIMP), it is easy to generate forged images at low cost. The localization of tampered regions turns out to be very tricky. Therefore, as the tampered images grow at an enormous rate, it is necessary to develop new algorithms against image forgery.

Media forensics has been developed to detect image forgeries for many years. However, few early works focused on forgery detection at pixel level. The researchers made great efforts in classifying whether an image has been tampered or not with traditional features, like wavelet transform feature [5], point matching [6], and self-consistency [7]. Furthermore, most of them detect only one specific type of manipulation, such as splicing [7], [8], copy-move [9], and removal [10]. Therefore, real-world media forensics is desperate for a new generation of algorithms which can obtain more refined results at pixel level, as well as the detection of general manipulations.

However, it is challenging to localize multiple image forgeries at pixel level since well-tampered images leaves no visual traces. Conventional detection methods based on manually constructed statistical features rely heavily on the domain knowledge of human experts.

Some early methods focused on low-level tampering artifacts in image forgeries, such as JPEG compression [11] and CFA color array analysis [12].

Recent works, including Mantra-Net [4], RGB-N [12], J-LSTM [13], H-LSTM [14], have proposed general and end-to-end solutions for image forgery localization using deep learning-based approaches. Both Wu *et al.* [4] and Zhou *et al.* [12] borrowed three high pass filters from Steganalysis Rich Model (SRM) [15] prior to their end-to-end framework to discover noise inconsistency between authentic and tampered regions. Specifically, Mantra-Net [4] is a joint system that predicts manipulation traces for both image manipulation classification and forgery localization. It employs a VGG-based [16] feature extractor to capture location information. Zhou [12] presented a two-stream network which consists of a regular RGB-based faster R-CNN stream and a parallel stream generated with SRM based noise extractor. The drawback of RGB-N is that it can only mark tampered regions with rectangular boxes due to the R-CNN structure. In the meantime,

*Corresponding author: Shunquan Tan.

All of the members are with the Guangdong Key Laboratory of Intelligent Information Processing, Shenzhen Key Laboratory of Media Security, Guangdong Laboratory of Artificial Intelligence and Digital Economy (SZ), Shenzhen Institute of Artificial Intelligence and Robotics for Society, China (email: zhuolong@email.szu.edu.cn; tansq, libin, jwhuang@szu.edu.cn).

S. Tan is with College of Computer Science and Software Engineering, Shenzhen University, Shenzhen 518060, China

This work was supported in part by the Key-Area Research and Development Program of Guangdong Province (2019B010139003), NSFC (61772349, U19B2022, 61872244), Guangdong Basic and Applied Basic Research Foundation (2019B151502001), and Shenzhen R&D Program (GJHZ20180928155814437, JCYJ20180305124325555). This work was also supported by Alibaba Group through Alibaba Innovative Research (AIR) Program.

Bappy *et al.* [13] applied an LSTM-based patch comparison method (J-LSTM) to detect the boundary of tampered and authentic patches and further presented a separate encoder-decoder structure (H-LSTM) [14] to improve the performance.

More recently, some approaches [17], [18], [19] used attention modules to focus on important regions in a target image. In the most recent one of them, Hu *et al.* [19] proposed a so-called SPAN model (Spatial Pyramid Attention Network), which is also selected in our work for comparison. The problem of all of the above mentioned attention-module based methods is that their key components are directly borrowed from object detection, and consequently are not well incorporated in forgery localization. For instance, their attention modules are object-sensitive and only pay attention to salient objects in an image. Since quite a few tampered regions are not objects in real scenario, traditional object attention modules might fail to guide networks' attention to tampered regions. Therefore, it is important to construct a novel network structure which can adapt attention mechanisms to forgery localization.

Furthermore, all state-of-the-art end-to-end solutions, e.g. SPAN [19], Mantra-Net [4], and RGB-N [12], have adopted normal data augmentation techniques, such as image flipping and rotation, to obtain twice or more number of training samples to avoid model over-fitting. However, with ultra limited training samples in this field, additional samples obtained with normal data augmentation is still limited. It is necessary to develop a new training strategy for forgery localization to increase sample number by one or two order of magnitude.

To address the above issues, we propose a novel framework and a self-adversarial training strategy toward the goal of localizing forged regions in images precisely. The proposed network involves a Channel-Wise High Pass Filter (CW-HPF) block and a *forgery attention* mechanism. Furthermore, we introduce the coarse-to-fine architecture to enhance network representations. Extensive experiments demonstrate that our approach have achieved state-of-the-art results on all primary benchmarks.

Specifically, CW-HPF splits an input feature map into channels. It then performs convolution initialized by three high pass filters, called HPF-Conv, on each channel to extract noise features, respectively. The HPF-Conv output is fused to uncover the inter-channel relationships of these noise features. The channel-wise architecture of CW-HPF is motivated by WISERNet [20], a powerful deep steganalysis model using inter-channel information.

On top of CW-HPF, we propose *forgery attention*, a novel attention mechanism considering forgery localization task. Inspired by the dual attention module [21], *forgery attention* aims to capture noise feature dependencies in both spatial and channel dimensions. In the spatial dimension, we extract spatial dependencies of noise features in every pixel pair of feature maps. Similarly, in the channel dimension, we capture channel dependencies of noise features among channel pairs. The outputs of two attentive dimensions are fused to enhance feature representations. *Forgery attention* enables our model to adaptively integrate local noise features with their global dependencies.

To alleviate the problem of limited training data, we present a novel Self-Adversarial Training (SAT) strategy for dynamical data augmentation. SAT exploits adversarial attacks [22] in every training iteration and generates new training data dynamically, which guides our model to defend from adversarial attacks and achieve more robust performance. Different from traditional data augmentation, our SAT can provide inexhaustible new adversarial training data according to model updating.

The remainder of the paper is organized as follows. In Section II, we present our proposed approach in details. Then, we show the results of our extensive experiments in Section III. Finally, we conclude this paper in Section IV.

II. PROPOSED APPROACH

In this section, we present the general framework of our proposed network as well as self-adversarial training strategy and then formulate our approach.

A. Overview

Given an image, we aim to localize its tampered regions at pixel level. The general framework of our proposed model is illustrated in Fig. 1. Furthermore, we propose self-adversarial training to promote the robustness of the network since forged training samples are ultra limited, whose details will be given in Sect. II-E.

Our network has a coarse-to-fine architecture. It is composed of two sub-networks, i.e., a *coarse net* and a *refined net*. The *coarse net* is fed with a forgery image I_F of size $H \times W \times 3$ and outputs a coarse prediction mask of size $H \times W$ and a feature map \hat{I}_{M_1} of size $H \times W \times k$, where k is set to 16 because the output of the last block outputs a feature map with 16 channels. The feature map \hat{I}_{M_1} is fed into the *refined net* that predicts a refined prediction mask I_M of size $H \times W$. Note that I_{M_1} and I_M come from two output convolution layers with a kernel size of 7×7 , activated by a sigmoid function. \hat{I}_{M_1} aims to deliver complete feature information to the *refined net*, which enables the *refined net* to be optimized along with the features. The predicted masks mark tampered regions in white and leave the rest in black. We select the refined mask I_M as the final result.

As illustrated in Fig. 1, there are three key components in the *coarse net*, including a CW-HPF block, multiple VGG-style blocks, and a series of dilated convolutional layers. The *refined net* adopts similar structure, but with a *forgery attention* module attached.

B. CW-HPF Block

HPF layer widely used in image steganalysis has been adopted in forgery localization [4], [12]. The intuition behind the usage of high-pass filters is that tampering traces are generally manifested in the middle and high frequency subbands of the tampered image. However, prior works have neglected the relationships among channels of images, which may yield many unnecessary noise features. To extract more accurate noise features, we leverage the inter-channel information to

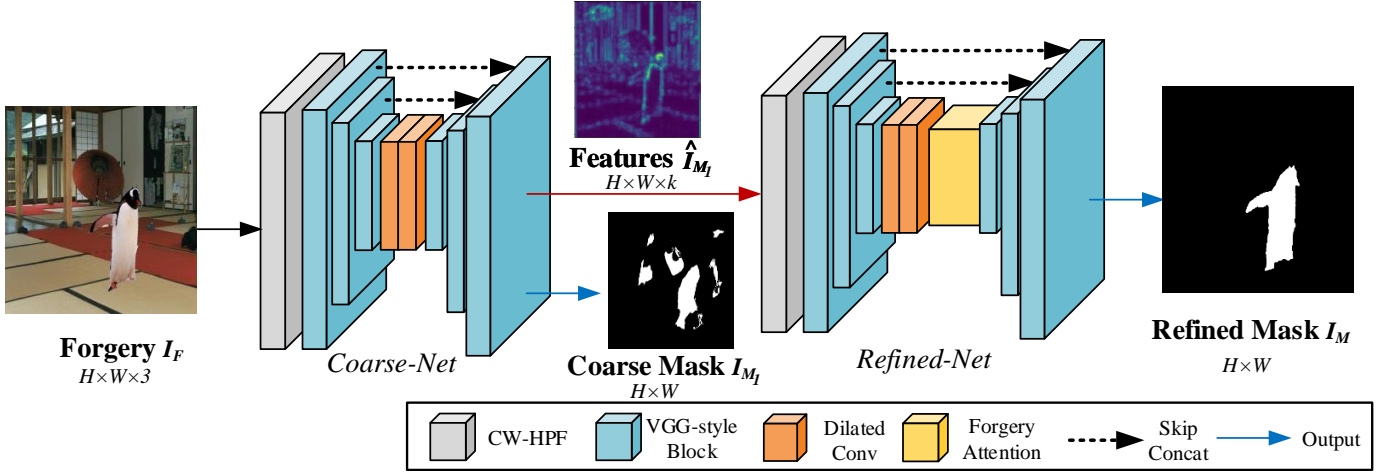


Fig. 1. Illustration of our proposed coarse-to-fine network for forgery localization task. It is composed of two sub-networks, namely coarse-net and refined-net. The coarse-net takes a forgery image I_F as input and predicts a coarse mask I_{M_1} and a feature map \hat{I}_{M_1} . The refined-net takes I_{M_1} and predicts a refined mask I_M .

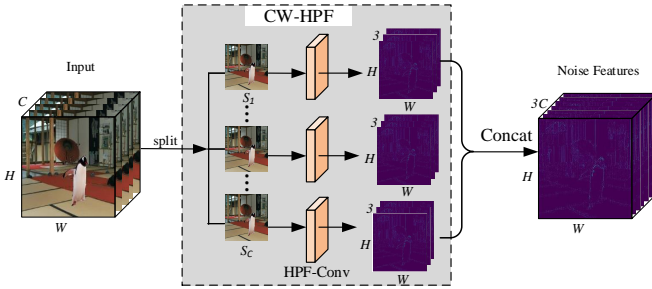


Fig. 2. Details of the Channel-Wise High Pass Filter (CW-HPF) block.

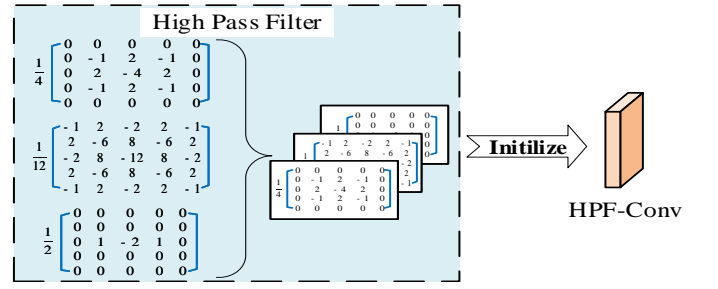


Fig. 3. Details of the High Pass Filter Convolution (HPF-Conv) layer.

enhance the noise inconsistency between tampered and pristine regions. Therefore, inspired by WISERNet [20], we propose CW-HPF block that extracts noise features incorporating channel-wise relationships.

Fig. 2 shows the details of the CW-HPF block. CW-HPF takes a feature map of size $H \times W \times C$ and outputs a noise feature map of size $H \times W \times 3C$. Firstly, the input feature map is converted to a feature map set \mathcal{S} with C feature maps. S_i represents the i -th channel of the input feature map. We define \mathcal{S} as $\mathcal{S} = \{S_1, S_2, S_3, \dots, S_C\}$. We employ three high pass filters originated from SRM [15] to initialize a convolution layer of size $5 \times 5 \times 3$, which we call HPF-Conv. As shown in Fig. 3, the selected high pass filters involve a KB filter, a KV filter and a first order kernel, which are the same as RGB-N [12]. Unlike steganalysis, the forgery localization task needs only three high pass filters from thirty steganalysis rich model filters to achieve decent performance and save computing resources [12]. We apply HPF-Conv to perform convolution with each element of the feature map set \mathcal{S} , and the results are concatenated to produce noise features of size $H \times W \times 3C$. CW-HPF in this work is unlearnable, and the filters are handcrafted.

C. Forgery Attention

Attention mechanism enables a neural network focus on important regions of its feature representations. Attention helps

it build input-aware connections to focus more on meaningful regions by replacing fixed weights with input dependent weights. Attention mechanism has been heavily involved in different application fields of deep-learning frameworks, such as machine translation [23], image captioning [24] and object detection [25]. Here, we propose a **forgery attention** mechanism to focus on tampered traces instead of salient objects in order to make it adapt to forgery localization tasks. The details of our forgery attention are formulated in Algorithm 1.

We construct two attention branches to obtain global noise attention features, as shown in Fig. 4. We feed local features $F \in \mathbb{R}^{H \times W \times C}$ generated by the dilated convolutional module of the *refined net* into two CW-HPF-based parallel attention branches, namely a **spatial attention branch** and a **channel attention branch**.

The *spatial attention branch* generates a Spatial-dimension Attention Feature map (denoted as SAF_N). It draws the spatial relationship between pairwise positions of the noise features. We update the features of each position by aggregating noise features of all positions with a weighted sum, where the weights are calculated by the similarities of the noise features between the corresponding two positions. For any two positions with similar noise features in the spatial dimension, they can contribute to mutual improvement.

Specifically, in the spatial dimension, the input F is fed into the CW-HPF block, followed by a convolution layer, to

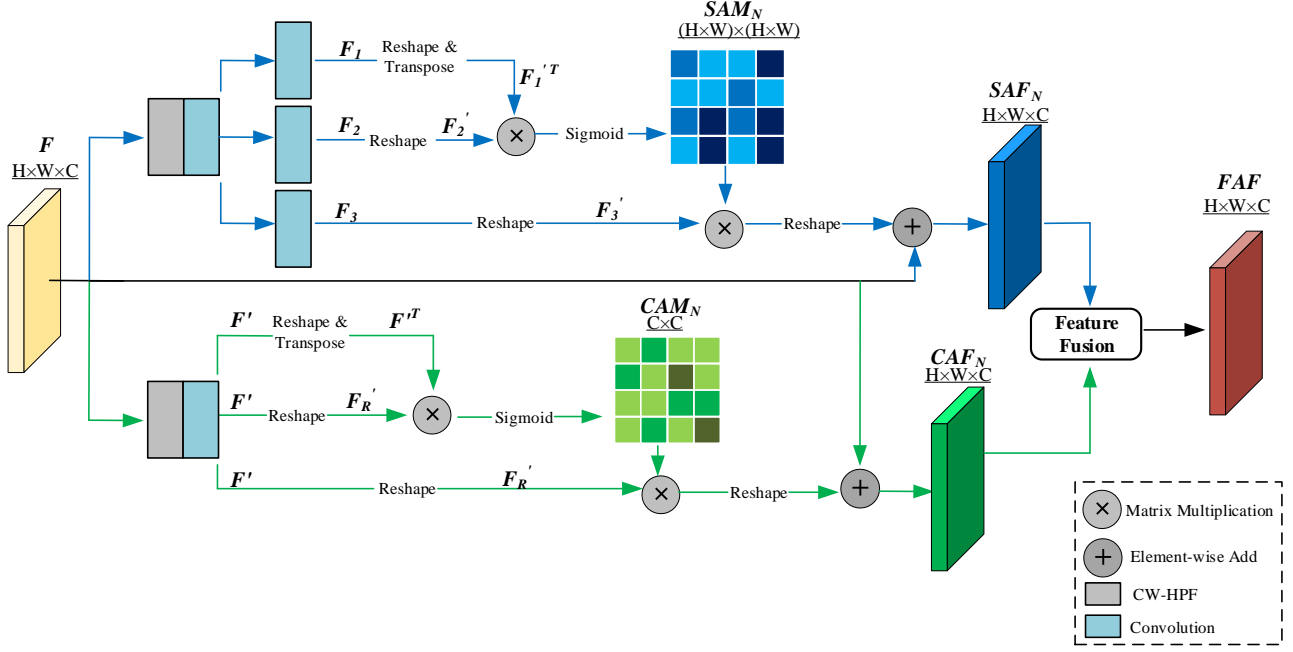


Fig. 4. The details of *forgery attention*. There are two parallel branches in *forgery attention*. The top one is the *spatial attention branch*, and the bottom one is the *channel attention branch*. Note that the cells with different darkness in SAM_N and CAM_N indicate the amount of attention paid to the noise features of these regions.

Algorithm 1 Forgery Attention Mechanism

Input: the feature map $F \in \mathbb{R}^{H \times W \times C}$;
Output: the Forgery Attention Feature $FAF \in \mathbb{R}^{H \times W \times C}$;
1: Initialize learnable parameters δ and γ ;
2: **for** every training iteration **do**
3: *Spatial attention branch:*
4: 1) Generate noise features using CW-HPF and a followed convolution layer;
5: 2) Generate F_1, F_2, F_3 using three parallel convolution layers;
6: 3) Reshape F_1 into $\mathbb{R}^{(H \times W) \times C}$;
7: 4) Transpose the result of 3) $\rightarrow F_1'^T \in \mathbb{R}^{C \times (H \times W)}$;
8: 5) Reshape $F_2 \rightarrow F_2' \in \mathbb{R}^{(H \times W) \times C}$;
9: 6) $Sigmoid(F_2' \times F_1'^T) \rightarrow SAM_N \in \mathbb{R}^{(H \times W) \times (H \times W)}$;
10: 7) Reshape $F_3 \rightarrow F_3' \in \mathbb{R}^{(H \times W) \times C}$;
11: 8) Reshape $\delta \cdot (SAM_N \times F_3')$ into $\mathbb{R}^{H \times W \times C}$;
12: 9) Element-wise addition of the result of 8) and $F \rightarrow SAF_N \in \mathbb{R}^{H \times W \times C}$;
13: *Channel attention branch:*
14: 1) Generate noise features F' using CW-HPF and a followed convolution layer;
15: 2) a) Reshape $F' \rightarrow F_R' \in \mathbb{R}^{(H \times W) \times C}$;
16: b) Transpose $F_R' \rightarrow F_R'^T \in \mathbb{R}^{C \times (H \times W)}$;
17: c) $Sigmoid(F_R'^T \times F_R') \rightarrow CAM_N \in \mathbb{R}^{C \times C}$;
18: d) Reshape $\gamma \cdot (CAM_N \times F_R')$ into $\mathbb{R}^{H \times W \times C}$;
19: e) Add the result of d) and $F \rightarrow CAF_N \in \mathbb{R}^{H \times W \times C}$;
20: 3) $SAF_N + CAF_N \rightarrow FAF$;
21: 4) Update δ and γ with back-propagation.
22: **end for**
23: **return** FAF

extract noise features. Three convolution layers are applied over the noise feature map in parallel to generate three feature maps $F_1, F_2, F_3 \in \mathbb{R}^{H \times W \times C}$, respectively. F_1, F_2 and F_3 are then reshaped to two-dimensional feature maps F_1', F_2' and F_3' , each of which belongs to $\mathbb{R}^{(H \times W) \times C}$. F_1' is further transposed to $F_1'^T \in \mathbb{R}^{C \times (H \times W)}$. Matrix cross product of F_2' and $F_1'^T$ is performed to calculate the distances between

different positions. Here, the result of the product measures the impact of i^{th} position on j^{th} position, where (i, j) in $((H \times W), (H \times W))$. The matrix cross product is further fed to a Sigmoid activation to get the Spatial Attention Matrix of noise features $SAM_N \in \mathbb{R}^{(H \times W) \times (H \times W)}$. SAM_N describes the similarity between any two different positions in the spatial dimension of the noise feature map. According to [21], the more similarity between two positions in the noise feature map is, the greater the correlation between two points in F becomes. SAM_N is then multiplied with F_3' , and the result is reshaped back to $H \times W \times C$. Finally, a learnable scaling factor γ is multiplied with the result of the last step and then is added with the input features F to generate $SAF_N \in \mathbb{R}^{H \times W \times C}$. It is formulated as follows:

$$SAF_N = \gamma(SAM_N \times F_3) + F$$

$$= \gamma(\text{sigmoid}(F_1'^T \times F_2') \times F_3') + F, \quad (1)$$

where we initialize γ as 0 and update it with back-propagation learning.

Meanwhile, the *channel attention branch* generates a Channel-dimension Attention Feature map (denoted as CAF_N) to model the channel relationship between any two channels of noise features. We update each channel feature map with a weighted sum of all channel feature maps.

The calculation in the channel dimension is similar to that in the spatial dimension. Firstly, a CW-HPF and a convolution layer are used to generate the noise features F' of input F , where $F' \in \mathbb{R}^{H \times W \times C}$. F' is reshaped to $F_R' \in \mathbb{R}^{(H \times W) \times C}$. F_R' is then performed matrix cross product with $F_R'^T$. A Sigmoid activation is applied to calculate the Channel Attention Matrix $CAM_N \in \mathbb{R}^{C \times C}$ of noise features. Like SAM_N , CAM_N describes the similarity between any two different

positions in the channel dimension of the noise feature map. Then F'_R is performed matrix cross product with CAM_N , whose result is reshaped to $H \times W \times C$. Finally, the matrix cross product result is multiplied by another learnable scaling factor δ , and the multiplication result is added with the input F to obtain $CAF_N \in \mathbb{R}^{H \times W \times C}$:

$$\begin{aligned} CAF_N &= \delta(CAM_N \times F'_R) + F, \\ &= \delta(\text{sigmoid}(F'^T \times F'_R) \times F_R) + F, \end{aligned} \quad (2)$$

where δ starts from 0 and gradually adjusts to assign more weight during training.

The introduction of the two learnable scaling factors, namely γ and δ , during the training procedure of SAF_N and CAF_N is borrowed from [21], in order to enhance network representation. In addition, please note that there are only two classes (i.e., forged or not) in the forgery localization task, and usually prediction of every pixel ranges from 0 to 1. Therefore, in **forgery attention**, SAF_N and CAF_N are generated with Sigmoid activation rather than traditional Softmax function since the value of Sigmoid activation is confined in [0,1].

After that, SAF_N and CAF_N are then fused to obtain the Forgery Attention Features (FAF). In particular, an element-wise addition is performed on SAF_N and CAF_N , of which the result is fed into a convolution layer to generate FAF. As a result, FAF provides the similarity map of noise features in both channel and spatial dimensions. It reflects long-term contextual information in the noise domain because any two positions with similar noise features can contribute mutual improvement regardless of their distance in both spatial dimension and channel dimension.

D. VGG Block and Dilated Convolutional Block

The architecture of VGG blocks originates from Mantra-Net [4]. Each VGG block contains three or four stacked convolution layers with kernel size 3×3 . In *coarse net*, the VGG modules are denoted as $\mathcal{V}_i(f)$ ($i \in \{1, 2, 3, 4, 5\}$), where f denotes the input features and \mathcal{V}_i denotes VGG block. \mathcal{V}_i performs encoding when $i = 1, 2, 3$ while performs decoding when $i = 4, 5$. The VGG blocks are of size 32×2^i when $i = 1, 2, 3$, and size $32 \times 2^{5-i}$ when $i = 4, 5$. Max pooling layers follow $\mathcal{V}_1(f)$ and $\mathcal{V}_2(f)$ to down-sample the features, and the output of them is skip-concatenated with that of $\mathcal{V}_5(f)$ and $\mathcal{V}_4(f)$, respectively. $\mathcal{V}_4(f)$ and $\mathcal{V}_5(f)$ are followed by up-sampling layers to restore the size of feature maps.

Zhuang *et al.* [26] has pointed out that for forgery localization task the deep-learning framework needs larger receptive fields to avoid learning features from narrow local regions. Thus following their approach, four dilated convolution layers are applied to inflate the kernels by inserting zeros between kernel elements with different dilation rates for extracting features with larger receptive fields. The dilated convolution layers are then used to bridge the encoders and the corresponding decoders in both the *coarse net* and the *refined net*. Specifically, the dilation rates in the four dilated convolution layers are 2, 4, 8, and 16, respectively.

Algorithm 2 Self-adversarial Training Strategy

Input: The tampered image I_F and y_{gt} , the corresponding binary mask of ground truth;

Output: The parameters θ of our network;

- 1: Initialize weights and biases of our network as illustrated in Fig. 1;
- 2: **for** every training iteration **do**
- 3: **(Begin Phase 1)**
- 4: Predict the coarse prediction mask I_{M_1} and the refined prediction mask I_M for the forgery image I_F ;
- 5: $[I_F, (I_{M_1}, I_M), (y_{gt}, y_{gt})] \Rightarrow \text{FirstTrainSet}$
- 6: Update parameters θ of our network with FirstTrainSet;
- 7: **(End Phase 1)**
- 8: **(Begin Phase 2)**
- 9: $\text{Random}(0, 0.01) \rightarrow \epsilon$;
- 10: Initialize FGSM algorithm (Equation 3) with ϵ and the updated θ ;
- 11: $\text{FGSM}(I_F, y_{gt}) \rightarrow I_{adv}$
- 12: Predict the coarse prediction mask I_{M_1} and the refined prediction mask I_M for the adversarial image I_{adv} ;
- 13: $[I_{adv}, (I_{M_1}, I_M), (y_{gt}, y_{gt})] \Rightarrow \text{SecondTrainSet}$
- 14: Update parameters θ of our network with SecondTrainSet;
- 15: **(End Phase 2)**
- 16: **end for**

E. Self-Adversarial Training

The pipeline of our proposed Self-Adversarial Training is shown in Fig. 5(a). SAT divides a single training iteration into two phases. The details of SAT are formulated in Algorithm 2.

In the first training phase, like the traditional training process, our model is trained on the original forgery image $I_F \in \mathbb{R}^{H \times W \times C}$ and its corresponding ground-truth mask y_{gt} .

In the second training phase, an adversarial image I_{adv} from I_F is firstly generated with the Fast Gradient Sign Method (FGSM) [22], a fast and famous adversarial attack method. FGSM attacks the latest gradients of our model to generate an adversarial example $I_{adv} \in \mathbb{R}^{H \times W \times C}$, which can be formulated as follows:

$$I_{adv} = I_F + \epsilon \cdot \text{sign}(\nabla_{I_F} L(\theta, I_F, y_{gt})), \quad (3)$$

where θ denotes the current parameters of our model, ∇_{I_F} denotes obtaining the gradients of our model when input I_F and L denotes the loss function. ϵ is taken a random number in range (0, 0.01] in every iteration to increase randomness. The model is then trained on the obtained adversarial example I_{adv} and y_{gt} , the corresponding ground-truth mask also used in the first training phase.

With two-phase self-adversarial training, SAT can provide new training data dynamically from limited original samples. Those training data generated via adversarial attacks, e.g. FGSM, can make our model more robust.

To illustrate the impacts of SAT, we draw the residual map between I_F and I_{adv} and then enlarge it by ten times, as shown in Fig. 5(a). The residual map will change in the following epoch because I_{adv} is constantly changing. Meanwhile, to differ the forgery image I_F and its corresponding adversarial example I_{adv} , we illustrate the inference results of them before training I_{adv} in Fig. 5(b). As shown in Fig. 5(b), before the second training phase, the model predicts an approximately precise mask using I_F but predicts a wrong mask using I_{adv} .

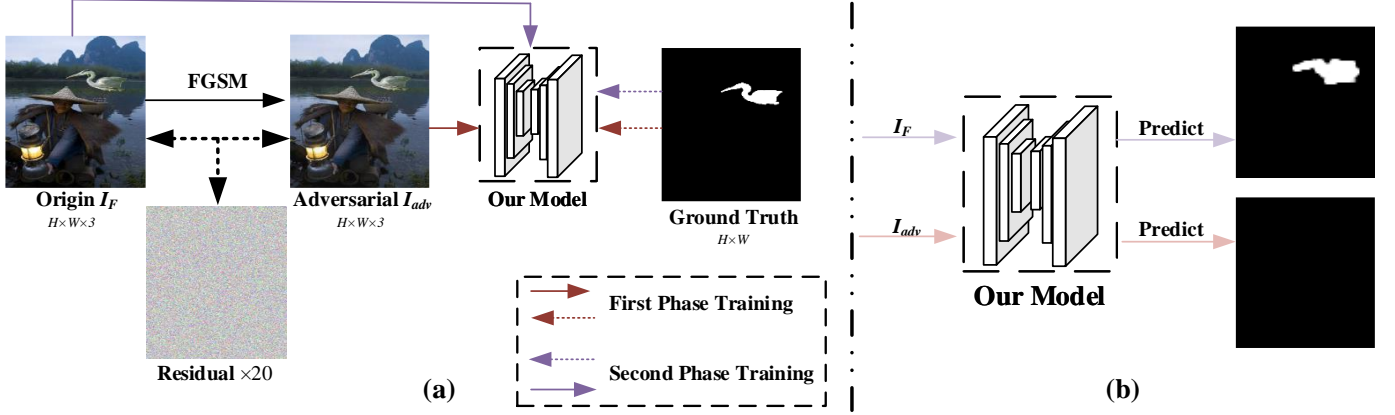


Fig. 5. Illustration of our proposed SAT. It trains our model in two phases. Fig. (a) shows the training procedure of SAT. Values of the residual map between I_F and I_{adv} are multiplied by 20 for better visualization. Fig. (b) shows different responses of our model prior to the second phase, when it is fed with I_F or fed with I_{adv} . The network predicts a totally black mask input I_{adv} while it predicts a roughly accurate mask input I_F .

F. Visualization Analysis

To explore the internal mechanism of our proposed CW-HPF and *forgery attention*, visualization analysis was conducted in this section. As illustrated in Fig. 6, a forgery image was taken as examples. We visualized the activation maps of different noise features extracted from a normal high pass filter layer [12] and our proposed CW-HPF. CW-HPF uses the inter-channel information while HPF does not. Then in Figs. 7 and 8, we visualized the activation maps of different attention feature maps predicted by a normal attention module [21] and our proposed *forgery attention*. The activation maps with heatmaps were super-imposed on the forgery image, where the red regions were with high activation values while the blue ones were with low values.

1) *CW-HPF*: As we can see in Fig. 6, it is clear that compared with original HPF, noise features generated by our proposed CW-HPF respond less to the pristine regions. CW-HPF mainly focuses on the tampered regions, which implies that CW-HPF extracts forgery relevant noise features more precisely.

The variance of each noise feature map was also calculated. As shown in Fig. 6, the variance σ^2 of our CW-HPF noise features is only one-ninth of that of HPF noise features, which also reveals that CW-HPF noise features have a smaller internal gap. The small variance enables CW-HPF to extract more consistent noise features in the tampered regions.

One possible reason of this phenomenon is that our CW-HPF takes advantage of inter-channel relationships to enhance the correlation between all channels. These relationships amplify the slight perturbations of noise inconsistency. Therefore CW-HPF focuses more on the tampered regions.

2) *Forgery Attention*: Figs. 7 and 8 visualize different regional attention of normal attention features and our proposed *forgery attention* features. Especially in Fig. 8, the redder regions in the heatmap of normal attention features fell in two persons while *forgery attention* had higher responses to the background. It indicates that the *forgery attention* focuses more on the tampered regions instead of the salient objects. That's because architectures of normal attention modules are

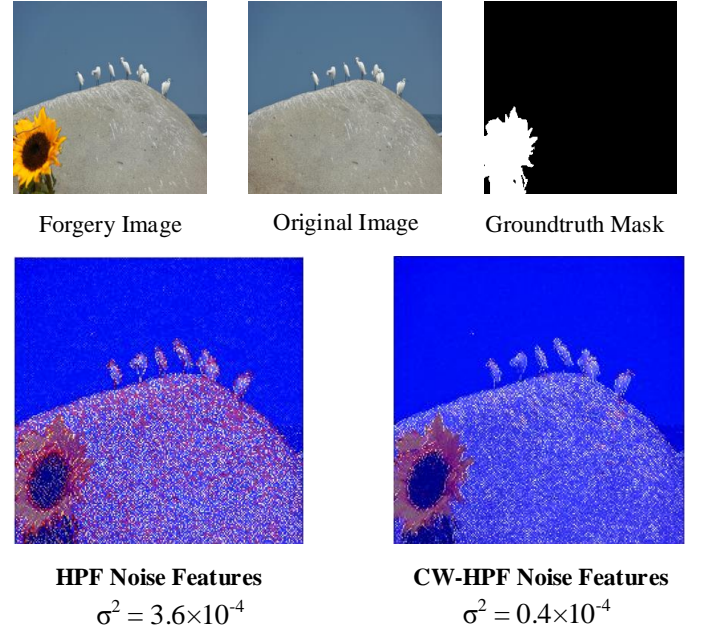


Fig. 6. Visualization of different noise features extracted from an example image (NIST2016_4867.jpg) from NIST. From the visualization we can observe that HPF noise features are highly responsive at rock and birds in red, which are pristine regions, while ours are not. It indicates that CW-HPF noise features respond weakly to pristine regions but more intensive on tampered regions.

designed to detect the texture of objects. On the contrary, our *forgery attention* aims to pay more attention to the tampered traces.

The possible reason why *forgery attention* aims to pay more attention to the tampered traces is that it explores global contextual noise information by building associations among noise features with the attention mechanism. In addition, it can also be attributed to CW-HPF which extracts the noise features first. Our method can adaptively aggregate long-term contextual information of noise features, thus improves feature representation for forgery localization.

Specifically, two attention branches contribute to focusing

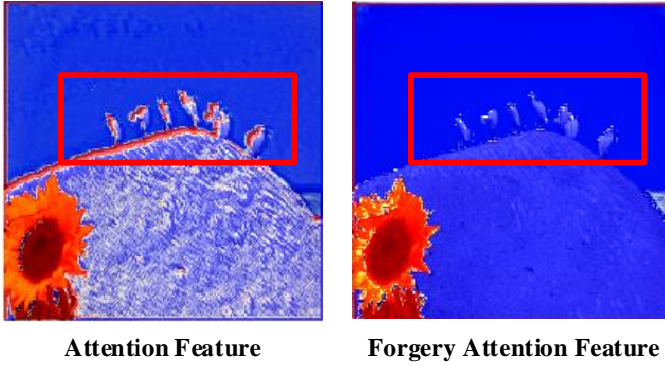


Fig. 7. Visualization of different attention features of the example image in Fig. 6. The red box emphasizes untampered objects, namely the birds. The untampered area of the left heatmap is redder than that of the right one, which indicates that the normal attention module responds to all objective regions while our *forgery attention* focuses more on the tampered regions.

on noise interdependencies. It can be inferred from Equation 1 that the resulting feature SAF_N at each position is a weighted sum of the noise features across all pixels and the original feature, which gives it a global contextual view and selectively aggregative contexts. Similar noise features achieve mutual gains, thus improving the noise consistency between the tampered and original regions. Furthermore, Equation 2 shows that the final feature of each channel is a weighted sum of the noise features of all channels and original features, which further models long-term noise dependencies among feature maps to boost noise feature discriminability. Each high-level channel can be regarded as a class-specific response, and different noise responses are associated with each other. Exploiting the interdependencies between channel maps emphasizes interdependent feature maps and improves the feature representation of tampered traces. Therefore, *forgery attention* achieves better performance in forgery localization tasks.

III. EXPERIMENTS

In this section, we carry out comprehensive experiments to demonstrate our proposed approach on several benchmark datasets and compare the results with state-of-the-art methods. Besides, we evaluate the robustness of our method in the scenarios of resizing, JPEG compression, and adversarial attacks. The source codes and auxiliary materials are available for download from GitHub¹.

A. Setup

1) *Datasets*: The following datasets are used in our experiments:

- **DEFACTO** [27] is a synthesized dataset generated from MSCOCO [28]. Three typical types of forgeries (i.e., splicing, copy-move, and removal) are involved in DEFACTO. 98,779 tampered images are selected from DEFACTO as our base dataset for ablation study and pre-training. We have to emphasize that our base dataset contains fewer images than other studies', such as Mantra-

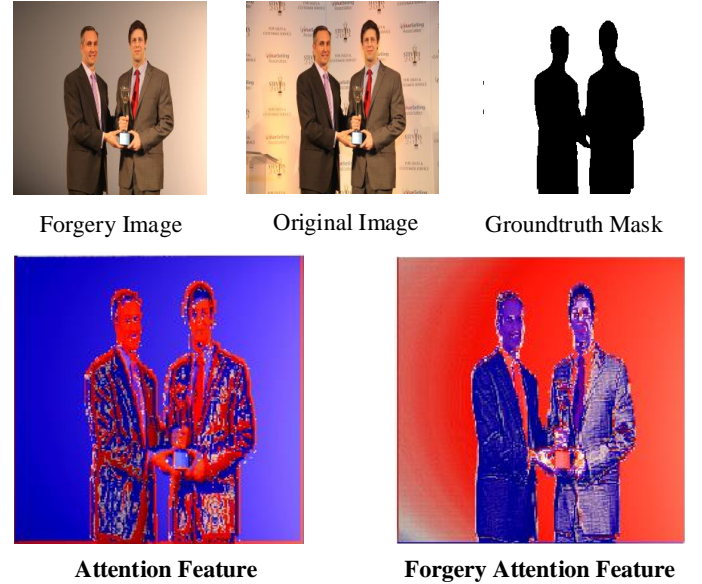


Fig. 8. Visualization of different attention features of an example image (NIST2016_3119.jpg) from NIST 2016. The normal attention module responds to the objects (i.e., persons) in red while our *forgery attention* responds more to the tampered regions (the background).

Net [4] (102,028 samples) and SPAN [19] (102,028 samples). The training-testing ratio is set to 9:1.

- **Columbia** [29] provides 180 splicing images with edge masks. The ground-truth masks are generated by ourselves from the corresponding edge masks
- **CASIA** [30] contains splicing and copy-move images in which forged regions are carefully selected. Some forged images have been further post-processed with filtering and blurring. It can be split into CASIA 2.0 (5,123 samples) for training and CASIA 1.0 (921 samples) for testing. Both of them are provided with ground-truth masks.
- **COVERAGE** [9] contains 100 forgery images manipulated by copy-moving. All the images are post-processed to remove visual traces. It is provided with ground-truth masks.
- **NIST** [31] is composed of 564 samples manipulated with splicing, copy-move, or removal. The visible traces of manipulations are concealed by post-processing. The dataset has ground-truth masks for evaluation.
- **PS-dataset** is a large-resolution dataset introduced in the latest work [26]. It involves three sub-datasets, namely PS-boundary dataset, PS-arbitrary dataset and PS-script dataset. Among these sub-datasets, PS-boundary dataset and PS-arbitrary dataset are created manually with Photoshop®, while PS-script dataset is tampered with automatic script.

Please note that for the sake of fair comparison, our experiments follow the training-testing ratio configuration in RGB-N [12] on NIST, COVERAGE, and CASIA.

2) *Implementation Details*: Our approach have been implemented based on TensorFlow. Our framework was trained with input images resized to 512×512 on a single Tesla P100

¹<https://github.com/tansq/SATFL>

TABLE I
QUANTITATIVE RESULTS OF ABLATION STUDIES ON DEFACTO.

Model	AUC	F_1
Baseline	0.978	0.855
CW-HPF Model	0.986	0.878
<i>Forgery Attention</i> Model	0.990	0.890
Coarse-to-fine <i>Forgery Attention</i> Model	0.992	0.904
Coarse-to-fine <i>Forgery Attention</i> Model+SAT	0.996	0.920
Coarse-to-fine <i>Forgery Attention</i> Model+SAT+Flipping+Rotation	0.998	0.929

GPU.² An ADAM solver were used to optimize the model with a learning rate of 0.002.

3) *Evaluation Metrics*: Pixel-level F_1 score and Area Under the receiver operating Curve (AUC) were employed as our evaluation metrics. F_1 score and AUC measured the performance of binary classification for every pixel, where higher scores indicate better performance. Both pixel-level AUC and F_1 score values range in [0,1]. Kindly note according to observations based on our experimental results, F_1 score is more accurate than AUC. This is due to the fact that F_1 score drops significantly when the predicted masks contains quite a few false-positive predictions (the pristine pixels are marked as tampered). On the contrary, AUC still remains at a high score on account of some factors such as threshold settings in this case.

4) *Loss Function*: During training, binary cross-entropy loss was used as our training loss function. It was minimized by optimizing the model parameters. The loss function is formulated as follows:

$$\text{Loss} = L_{\text{BCE}}(y_{\text{gt}}, y_{M_1}) + L_{\text{BCE}}(y_{\text{gt}}, y_M), \quad (4)$$

where L_{BCE} denotes Binary Cross-Entropy loss, y_{gt} denotes ground-truth masks, y_{M_1} denotes coarse masks, and y_M denotes refined masks.

B. Ablation Study

Ablative experiments were conducted on the DEFACTO dataset to validate our proposed components and SAT. The setup models were as follows:

- **Baseline**: The baseline model contained an HPF filter layer, a dilated convolutional module, and VGG blocks. It did not have a coarse-to-fine architecture.
- **CW-HPF Model**: The HPF filter layer was replaced in the baseline model with a CW-HPF filter block. Others remained the same.
- **Forgery Attention Model**: It was constructed based on the CW-HPF model, composed of CW-HPF, VGG blocks, a dilated convolutional module, and a *forgery attention* module.
- **Coarse-to-fine Forgery Attention Model**: A coarse-to-fine net was constructed using the CW-HPF model as the *coarse net* and *forgery attention* model as the *refined net*. This is actual our proposed model.

All models were trained using the same setting, and the results are reported in Table I. From Table I, it can be seen that our proposed components are all effective and improve the AUC and F_1 scores significantly. The CW-HPF block improves the performance by 0.008 in AUC and 0.023 in F_1 . The *forgery attention* module further improves by 0.004 in AUC and 0.012 in F_1 over the CW-HPF model. The coarse-to-fine architecture further improves by 0.002 in AUC and 0.014 in F_1 over the *forgery attention* model.

Furthermore, to evaluate our proposed self-adversarial training strategy, data augmentation techniques were applied for the well-trained coarse-to-fine forgery attention model, namely our proposed SAT plus flipping and rotation. As also shown in Table I, our proposed SAT further boosts the performance by 0.004 in AUC and 0.016 in F_1 . SAT provides dynamic training data for more robust performance. For optimal performance, flipping and rotation were employed to further augment the training dataset and achieve 0.998 in AUC and 0.929 in F_1 .

C. Quantitative Results Compared against State-of-the-art Methods

We compare the performance of our framework against several related methods on four benchmarks, namely NIST, COVERAGE, Columbia, and CASIA. The related methods include classic unsupervised methods, such as ELA [32], NOI1 [33], and CFA1 [34], and the latest deep networks, including H-LSTM [14], RGB-N [12], Mantra-Net [4], and SPAN [19]. We evaluated our framework under different setups: (1) benchmark training only; (2) fine-tuning. Under the benchmark training only setup, our model was trained on each benchmark separately. Under the fine-tuning setup, to achieve optimal performance, our pre-trained model was fine-tuned using several benchmarks, including NIST, COVERAGE, and CASIA, and tested on the corresponding testing split. Note that a training-testing ratio was set to 7:3 during benchmark training on the Columbia dataset. The actual reason has been given in accompanying discussions of Table II.

The results are reported in Table II. When adopting the benchmark training setup that uses only a small amount of training data, e.g., 75 forgery images from COVERAGE, our model shows superior performance compared to state-of-the-art approaches, especially on the Columbia dataset where our F_1 score outperforms all other methods. It indicates that our approach does not rely on large-scale training data to achieve decent performance, which shows the effectiveness of our approach. In the fine-tuning setup, our approach takes

²OpenCV package was used to resize the images. We set interpolation=INTER_AREA when resizing the forgery images and set interpolation=INTER_NEAREST for resizing the masks.

TABLE II
QUANTITATIVE RESULTS COMPARED AGAINST RELATED METHODS.

Method	Training Method	NIST		COVERAGE		Columbia		CASIA	
		AUC	F_1	AUC	F_1	AUC	F_1	AUC	F_1
ELA	unsupervised	0.429	0.236	0.583	0.222	0.581	0.470	0.613	0.214
NOI	unsupervised	0.487	0.285	0.587	0.269	0.546	0.574	0.612	0.263
CFA1	unsupervised	0.501	0.174	0.485	0.190	0.720	0.467	0.522	0.207
H-LSTM	fine-tuning	0.794	—	0.712	—	—	—	—	—
RGB-N	fine-tuning	0.937	0.722	0.817	0.437	0.858	0.697	0.795	0.408
Mantra-Net	pre-training	0.795	—	0.819	—	0.824	—	0.817	—
SPAN	fine-tuning	0.961	0.582	0.937	0.558	0.936	0.815	0.838	0.382
Ours	benchmark training	0.943	0.622	0.856	0.526	0.917	0.891	0.788	0.384
Ours	finetuning	0.990	0.878	0.985	0.843	0.999*	0.983*	0.843	0.592

good advantage of large-scale training data. It can be concluded that our approach is further boosted by large-scale training data. In particular, our approach outperforms SPAN by 0.296 in F_1 score on NIST dataset and 0.048 in AUC on COVERAGE dataset. Note that because all of the forged regions in Columbia dataset are large while the forged regions in DEAFCTO are small ones. Thus, there is a domain gap between Columbia and DEAFCTO. So different from the settings of SPAN and Mantra-Net, our results on Columbia dataset are based on 30% testing data and other 70% data is used for finetuning. It is clear from Table II that our model that is trained on DEFACTO dataset and finetuned on each benchmark datasets achieves state-of-the-art performance. The possible reason is that the proposed components and SAT training strategy work jointly and achieve optimal performance.

Furthermore we compare the effectiveness of our model with the most recent algorithm, i.e., dense fully convolutional network (DFCN) [26]. We followed this setting [26] and used 512×512 image patches for training while full images for testing. Our model was trained using PS-script dataset and finetuned using only 10% forged images of several datasets, respectively, i.e., 100 samples in PS-arbitrary dataset, 100 samples in PS-boundary dataset and 56 samples in NIST dataset. Note that in the setting of [26], which is different from our experiments on NIST dataset in Table II, NIST dataset is split into 512×512 patches. It can be seen from the Table III that the performance of our model outperforms DFCN on three datasets. Before fine-tuning in each benchmark datasets, our results are slightly lower than DFCN in AUC on PS-arbitrary and NIST datasets. However, our model has been over DFCN by 0.01 in AUC on PS-boundary dataset. About F_1 score, our results are about 25% higher on PS-boundary dataset and 15% higher on NIST than DFCN's. After fine-tuning in each datasets, our method has make a good improvement and outperforms DFCN on three datasets. In particular, our results achieve about 10% in F_1 score higher on PS-boundary dataset, slightly higher in AUC and F_1 score on PS-arbitrary dataset, and about 6% in AUC on NIST dataset than DFCN.

D. Qualitative Results

In Fig. 9, we show the prediction masks of our proposed framework for some selected images. From Fig. 9, it can

TABLE III
QUANTITATIVE RESULTS AGAINST THE MOST RECENT ALGORITHM, DFCN. OUR ALGORITHM WAS FINETUNED USING 100 SAMPLES IN PS-ARBITRARY DATASET, 100 SAMPLES IN PS-BOUNDARY DATASET AND 56 SAMPLES IN NIST DATASET, RESPECTIVELY.

Method	PS-boundary		PS-arbitrary		NIST	
	AUC	F_1	AUC	F_1	AUC	F_1
DFCN (w/o fine-tuning)	0.90	0.61	0.91	0.57	0.63	0.20
Ours (w/o fine-tuning)	0.91	0.76	0.90	0.58	0.61	0.23
DFCN (fine-tuning)	0.99	0.82	0.97	0.67	0.80	0.38
Ours (fine-tuning)	0.99	0.90	0.98	0.69	0.85	0.40

TABLE IV
ROBUSTNESS ANALYSIS OF OUR FRAMEWORK ON THE NIST DATASET. THE RESULTS ARE REPORTED IN PIXEL-LEVER AUC.

Manipulations	Mantra-Net	SPAN	Ours
None	0.795	0.8395	0.990
Resize (0.78x)	0.7743	0.8324	0.984
Resize (0.25x)	0.7552	0.8032	0.979
GaussianBlur (kernel size=3)	0.7746	0.8310	0.983
GaussianBlur (kernel size=5)	0.7455	0.7915	0.951
GaussianNoise (sigma=3)	0.6741	0.7517	0.937
GaussianNoise (sigma=15)	0.5855	0.6728	0.866
JPEGCompress (quality=100)	0.7791	0.8359	0.978
JPEGCompress (quality=50)	0.7438	0.8068	0.938
FGSM (eps=0.02)	0.5058	—	0.986

be seen that our approach produces accurate results against different tampering techniques. No matter whether they are tampered objects or background without recognizable objects such as *snow*, our method detects them with high precision. In terms of processing speed, our framework, takes roughly 126ms per image of size 512×512 on a single Tesla P100 GPU.

E. Robustness Experiments

Robustness experiments of our framework was conducted in this section. OpenCV built-in functions (including **AREAResize**, **GaussianBlur**, **GaussianNoise**, and **JPEGCompress**) and adversarial attacks (**FGSM**) were employed to generate content-preserving manipulations on NIST. Note that epsilons

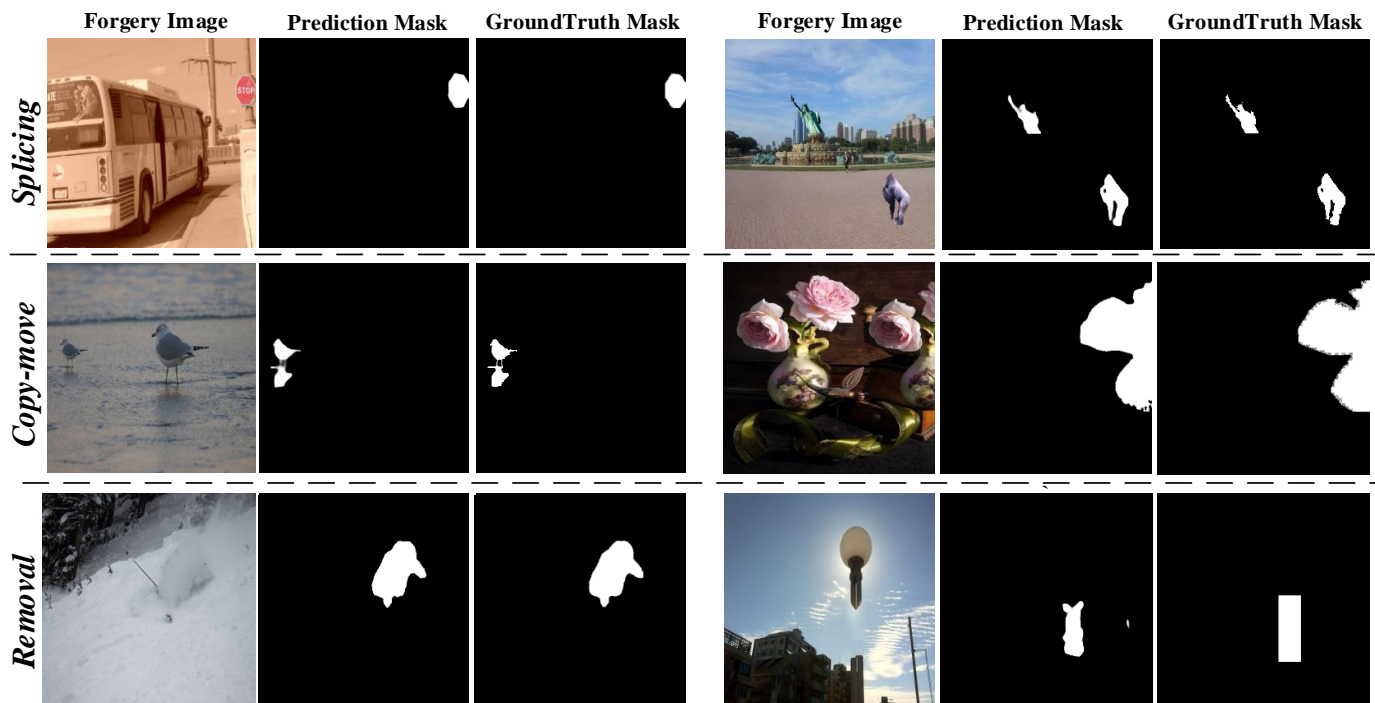


Fig. 9. Sample results of our framework in three popular manipulations, namely splicing, copy-move, and removal. The samples are from NIST, Columbia, COVERAGE, CASIA, and DEFACTO.

of FGSM used in our SAT strategy valued from 0 to 0.01 while the epsilon was 0.02 in testing stage, which is a fair comparison. As shown in Table IV, our framework is quite immune to several types of attacks. All results except FGSM of SPAN are reported in SPAN [19]. Because the SPAN code has not been released, we did not compare robustness on adversarial attacks with it.

IV. CONCLUSION

In this paper, we propose a novel deep neural network solution and a self-adversarial training strategy to effectively localize tampered regions in an image. The major contributions of our work are as follows:

- We have proposed a novel attention mechanism adapting to forgery localization task, named *forgery attention* which can be used to effectively capture noise feature dependencies in both spatial and channel dimensions.
- We have presented a novel self-adversarial training strategy for forgery localization, which augments training data dynamically to enable our model to achieve more robust performance, and alleviates the problem of limited labeled training data in this scenario.
- We have proposed a novel forgery localization framework in a coarse-to-fine manner, equipped with the Channel-Wise High Pass Filter (CW-HPF) block. Extensive experiments conducted on de-facto benchmarking datasets demonstrate that our approach outperform other state-of-the-art solutions in the literature by a clear margin.

Our future work will mainly focus on two aspects: (1) introduction of few-shot learning and even unsupervised learning based strategies to further tackle the issue of limited training

data; (2) further exploration of the feasibility of our proposed approach in wider multimedia forensics applications, e.g., video forgery localization and deepfake detection.

REFERENCES

- [1] L. Verdoliva, "Media forensics and deepfakes: An overview," *IEEE Journal of Selected Topics in Signal Processing*, vol. 14, no. 5, pp. 910–932, 2020.
- [2] T. M. Ghanim and A. M. Nabil, "Offline signature verification and forgery detection approach," in *Proceedings of the 13th International Conference on Computer Engineering and Systems*, 2018, pp. 293–298.
- [3] E. M. Bik, A. Casadevall, and F. C. Fang, "The prevalence of inappropriate image duplication in biomedical research publications," *mBio*, vol. 7, no. 3, 2016. [Online]. Available: <https://mbio.asm.org/content/7/3/e00809-16>
- [4] Y. Wu, W. AbdAlmageed, and P. Natarajan, "Mantra-net: Manipulation tracing network for detection and localization of image forgeries with anomalous features," in *Proceedings of the IEEE Conference on Computer Vision and Pattern Recognition*, 2019, pp. 9543–9552.
- [5] G. Muhammad, M. Hussain, and G. Bebis, "Passive copy move image forgery detection using undecimated dyadic wavelet transform," *Digital Investigation*, vol. 9, no. 1, pp. 49–57, 2012.
- [6] C.-M. Pun, X.-C. Yuan, and X.-L. Bi, "Image forgery detection using adaptive oversegmentation and feature point matching," *IEEE Transactions on Information Forensics and Security*, vol. 10, no. 8, pp. 1705–1716, 2015.
- [7] M. Huh, A. Liu, A. Owens *et al.*, "Fighting fake news: Image splice detection via learned self-consistency," in *Proceedings of the European Conference on Computer Vision*, 2018, pp. 101–117.
- [8] R. Salloum, Y. Ren, and C.-C. J. Kuo, "Image splicing localization using a multi-task fully convolutional network (MFCN)," *Journal of Visual Communication and Image Representation*, vol. 51, pp. 201–209, 2018.
- [9] B. Wen, Y. Zhu, R. Subramanian *et al.*, "COVERAGE—a novel database for copy-move forgery detection," in *Proceedings of IEEE International Conference on Image Processing*, 2016, pp. 161–165.
- [10] X. Zhu, Y. Qian, X. Zhao *et al.*, "A deep learning approach to patch-based image inpainting forensics," *Signal Processing: Image Communication*, vol. 67, pp. 90–99, 2018.

- [11] T. Bianchi, A. De Rosa, and A. Piva, "Improved DCT coefficient analysis for forgery localization in JPEG images," in *Proceedings of the IEEE International Conference on Acoustics, Speech and Signal Processing*. IEEE, 2011, pp. 2444–2447.
- [12] P. Zhou, X. Han, V. I. Morariu *et al.*, "Learning rich features for image manipulation detection," in *Proceedings of the IEEE Conference on Computer Vision and Pattern Recognition*, 2018, pp. 1053–1061.
- [13] J. H. Bappy, A. K. Roy-Chowdhury, J. Bunk *et al.*, "Exploiting spatial structure for localizing manipulated image regions," in *Proceedings of the IEEE International Conference on Computer Vision*, 2017, pp. 4970–4979.
- [14] J. H. Bappy, C. Simons, L. Nataraj *et al.*, "Hybrid LSTM and encoder-decoder architecture for detection of image forgeries," *IEEE Transactions on Image Processing*, vol. 28, no. 7, pp. 3286–3300, 2019.
- [15] J. Fridrich and J. Kodovsky, "Rich models for steganalysis of digital images," *IEEE Transactions on Information Forensics and Security*, vol. 7, no. 3, pp. 868–882, 2012.
- [16] K. Simonyan and A. Zisserman, "Very deep convolutional networks for large-scale image recognition," *arXiv preprint arXiv:1409.1556*, 2014.
- [17] A. Islam, C. Long, A. Basharat *et al.*, "DOA-GAN: Dual-order attentive generative adversarial network for image copy-move forgery detection and localization," in *Proceedings of the IEEE Conference on Computer Vision and Pattern Recognition*, 2020, pp. 4676–4685.
- [18] Y. Zhu, C. Chen, G. Yan *et al.*, "AR-Net: Adaptive attention and residual refinement network for copy-move forgery detection," *IEEE Transactions on Industrial Informatics*, vol. 16, no. 10, pp. 6714–6723, 2020.
- [19] X. Hu, Z. Zhang, Z. Jiang *et al.*, "SPAN: Spatial pyramid attention network for image manipulation localization," in *Proceedings of the European Conference on Computer Vision*, 2020, pp. 312–328.
- [20] J. Zeng, S. Tan, G. Liu *et al.*, "WISERNet: Wider separate-then-reunion network for steganalysis of color images," *IEEE Transactions on Information Forensics and Security*, vol. 14, no. 10, pp. 2735–2748, 2019.
- [21] J. Fu, J. Liu, H. Tian *et al.*, "Dual attention network for scene segmentation," in *Proceedings of the IEEE Conference on Computer Vision and Pattern Recognition*, 2019, pp. 3146–3154.
- [22] I. J. Goodfellow, J. Shlens, and C. Szegedy, "Explaining and harnessing adversarial examples," *arXiv preprint arXiv:1412.6572*, 2014.
- [23] A. Vaswani, N. Shazeer, N. Parmar *et al.*, "Attention is all you need," in *Advances in Neural Information Processing Systems*, 2017, pp. 5998–6008.
- [24] K. Xu, J. Ba, R. Kiros *et al.*, "Show, attend and tell: Neural image caption generation with visual attention," in *International Conference on Machine Learning*, 2015, pp. 2048–2057.
- [25] X. Li, W. Wang, X. Hu *et al.*, "Selective kernel networks," in *Proceedings of the IEEE Conference on Computer Vision and Pattern Recognition*, 2019, pp. 510–519.
- [26] P. Zhuang, H. Li, S. Tan *et al.*, "Image tampering localization using a dense fully convolutional network," *IEEE Transactions on Information Forensics and Security*, vol. 16, pp. 2986–2999, 2021.
- [27] G. Mahfoudi, B. Tajini, F. Retraint *et al.*, "DEFACTO: Image and face manipulation dataset," in *Proceedings of the 27th European Signal Processing Conference*, 2019, pp. 1–5.
- [28] T. Y. Lin, M. Maire, S. Belongie *et al.*, "Microsoft coco: Common objects in context," in *Proceedings of the European Conference on Computer Vision*, 2014.
- [29] T.-T. Ng, J. Hsu, and S.-F. Chang, "Columbia image splicing detection evaluation dataset," *DVMM lab. Columbia Univ CalPhotos Digit Libr*, 2009.
- [30] J. Dong, W. Wang, and T. Tan, "CASIA image tampering detection evaluation database," in *Proceedings of the IEEE China Summit and International Conference on Signal and Information Processing*, 2013, pp. 422–426.
- [31] H. Guan, M. Kozak, E. Robertson *et al.*, "MFC datasets: Large-scale benchmark datasets for media forensic challenge evaluation," in *Proceedings of the IEEE Winter Applications of Computer Vision Workshops*, 2019, pp. 63–72.
- [32] N. Krawetz and H. F. Solutions, "A picture's worth," *Hacker Factor Solutions*, vol. 6, no. 2, p. 2, 2007.
- [33] B. Mahdian and S. Saic, "Using noise inconsistencies for blind image forensics," *Image and Vision Computing*, vol. 27, no. 10, pp. 1497–1503, 2009.
- [34] P. Ferrara, T. Bianchi, A. De Rosa *et al.*, "Image forgery localization via fine-grained analysis of CFA artifacts," *IEEE Transactions on Information Forensics and Security*, vol. 7, no. 5, pp. 1566–1577, 2012.